

Article

Wind Field Distribution of Multi-rotor UAV and Its Influence on Spectral Information Acquisition of Rice Canopies

Lei Feng ^{1,2}, Weikang Wu ¹, Junmin Wang ³, Chu Zhang ¹ , Yiyang Zhao ¹, Susu Zhu ¹ and Yong He ^{1,2,*} 

¹ College of Biosystems Engineering and Food Science, Zhejiang University, 866 Yuhangtang Road, Hangzhou 310058, China; Lfeng@zju.edu.cn (L.F.); wwk@zju.edu.cn (W.W.); chuzh@zju.edu.cn (C.Z.); zhaoyy@zju.edu.cn (Y.Z.); sszhu@zju.edu.cn (S.Z.)

² Key Laboratory of Spectroscopy Sensing, Ministry of Agriculture and Rural Affairs, Hangzhou 310058, China

³ Institute of Crop Science and Nuclear Technology Utilization, Zhejiang Academy of Agricultural Sciences, Hangzhou 310021, China; wangjm917@sina.com

* Correspondence: yhe@zju.edu.cn; Tel.: +86-571-8898-2825

Received: 25 January 2019; Accepted: 7 March 2019; Published: 13 March 2019



Abstract: Unmanned aerial vehicles (UAV) are widely used as remote sensing platforms to effectively monitor agricultural conditions. The wind field generated by the rotors in low-altitude operations will cause the deformation of rice crops, and may affect the acquisition of the true spectral information. In this study, a low-altitude UAV remote sensing simulation platform and a triple-direction wind field wireless sensor network system were built to explore the wind field distribution law. Combined with the multi-spectral images of the rice canopy, the influence of wind field on the spectral information acquisition was analyzed through variance and regression analysis. The results showed that the Z-direction wind field of UAV rotors dominated along three directions (X, Y, and Z). The coefficient of determination (R^2) of three linear regression models for Normalized Difference Vegetation Index (NDVI), Ratio Vegetation Index (RVI), and Canopy Coverage Rate (CCR) was 0.782, 0.749, and 0.527, respectively. Therefore, the multi-rotor UAV wind field had an impact on the spectral information acquisition of rice canopy, and this influence could eventually affect the assessment of rice growth status. The models established in this study could provide a reference for the revised model of spectral indices, and offer guidance for the actual operations of low-altitude multi-rotor UAV.

Keywords: multi-rotor UAV; wind-field distribution; triple-direction wind field wireless sensor network; multispectral information

1. Introduction

The advantages of low cost, high efficiency, and being environment-friendly make small UAVs widely used in agriculture, especially for agricultural UAV remote sensing [1–3]. Combing with advance spectral imaging technique [4,5], agricultural UAV remote sensing can monitor farm crop growth in real time, generating a farmland crop prescription map based on high-resolution spectral images, which plays an important role in monitoring crop growth. However, low-altitude remote sensing operations are bound to affect the ground crops because of the rotor wind field. The UAV rotor wind field [6–10] is formed by the rotation of the rotor to promote the air flow in the crop canopy. The distribution of the wind field is often related to the flight parameters of the drone, the surrounding environment, and the distribution of the ground sensor, which is a multi-factor parameter. Experts and scholars have carried out a lot of studies on wind field measurement, and designed

a lot of wind field measurement systems with different principles. Wang et al. [11] deduced the inversion theoretical model of wind speed and temperature for the atmospheric wind field detection system based on a Fabry-Perot interferometer and theoretically verified it. Li et al. [12] designed a method for simulating and measuring an atmospheric wind field with simple equipment by using the modulation characteristics of a semiconductor laser and the high spectral resolution Fabry-Perot interferometer, which can effectively analyze and evaluate the Doppler wind speed measurement principle, data processing method, system performance, and measurement error. Ren et al. [13] performed an error analysis on the drone-static tube wind measurement of the UAV. The wind speed parameter acquisition system comprised an air speed sensor array and a wind speed data receiving end placed near the canopy of the field crop. The wind speed sensor array could sequentially transmit the collected wind speed values to the receiving end, and finally transmit these to the ground station for further processing.

In order to realize the multi-point, multi-wind direction, movable, and real-time acquisition of wind-related parameters of the UAV rotor airflow in the crop canopy, Hu et al. [14] designed a UAV wind field wireless sensor network measurement system that consisted of a number of triple-direction wind speed sensor wireless measurement nodes (WWSS), a UAV position and attitude measurement module (FGPS), and an intelligent master control aggregation module (ICFN). This system has been widely used for UAV wind field estimation and description, including this research. Li et al. [15,16] used the triple-direction wind field wireless sensor network measurement system to explore the distribution law of the wind field of the rotary-wing UAV pollination operation and optimize the parameters of assisted pollination operation by the circular multi-rotor electric UAV. Chen et al. [17] measured the wind field distribution under the rotor of the multi-rotor electric drone through the UAV rotor wind field to reveal the influence mechanism of the wind field under the rotor of the multi-rotor UAV on the droplet deposition distribution. To obtain better parameters of flight operation for auxiliary pollination, Wang et al. [18] used the wind field wireless sensor network measurement system to measure the wind field of the unmanned single-rotor helicopter in the paddy field, providing research support for rice seed production and auxiliary pollination.

So far, a lot of research and exploration has been carried out on the measurement and distribution law of the UAV wind field. However, most of them have focused on the field of pollination and air spray, and few studies have explored the effect of wind field disturbance on the collection of rice canopy spectral information. Based on the UAV simulation platform [19], this study measured the distribution of wind fields under the rotors of different altitudes through the triple-direction wind field wireless sensor network system, and the multispectral images of rice canopies were taken at different measurement points under the wind field. To explore the influence of a multi-rotor UAV wind field on rice canopy spectral information collection, the correlation between the triple-direction wind field under the rotor and the spectral information of the rice canopy was analyzed through variance and regression analysis, which provides a theoretical basis for scientific assessment and monitoring of rice crop growth.

2. Materials and Methods

2.1. Plant

A batch of selected rice seeds were sown in the paddy fields of Zhejiang Academy of Agricultural Sciences (Hangzhou, China). Selected rice plants of uniform size and good health were transplanted into containers with a mixture of organic soil and pine bark at the seedling stage. The plants were grown in a greenhouse at 20 ± 3 °C with a relative humidity (RH) of $70 \pm 5\%$. Plants were cultivated by ordinary daily watering and fertilization.

2.2. Instrument

The UAV simulation system was equipped with a F450 quadrotor UAV (Figure 1a) as the UAV remote sensing platform. The main performance indicators of the F450 UAV are shown in Table 1. The Tetracam Agricultural Digital Camera (ADC) was selected as the UAV imaging sensor (Figure 1b). It was a 3.0 megapixel (DCM format) agricultural digital camera with a maximum resolution of 2048×1536 pixels, and the image capture rate is approximately 1.0 to 7.5 s between consecutive images, depending upon image format and resolution selected. The specific parameters of the Tetracam ADC multispectral camera are shown in Table 1.

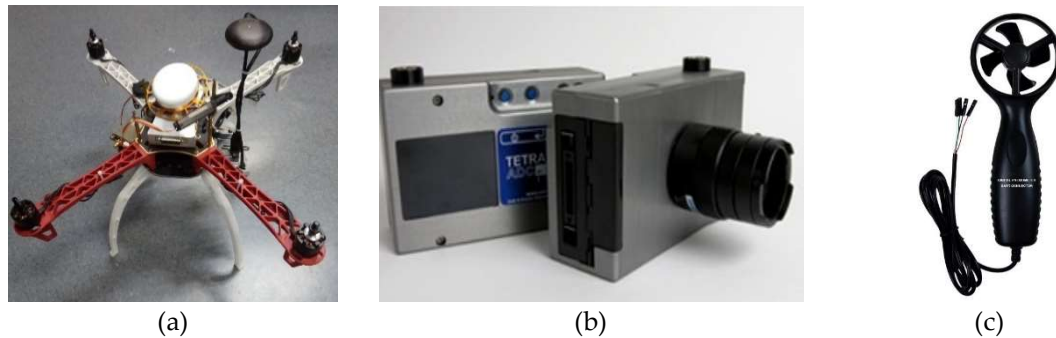


Figure 1. Experimental instruments: (a) F450 quadrotor UAV (Unmanned Aerial Vehicles); (b) Tetracam ADC (Agricultural Digital Camera); and (c) GM8904 digital interface impeller anemometer.

Table 1. Parameters of experimental UAV and Tetracam ADC.

	Items	Parameters
UAV	Model	F450 quadrotor UAV
	Weight	1.1 kg
	Pitch	4.7 inches
	Motor Diameter	10 inches
	Wheel base	45 inches
	Rotor Number	4
Tetracam ADC	Resolution	2048×1536 pixels
	Wave band	NIR (Near Infrared Ray, TM4), R (Red, TM3), G (Green, TM2)
	Exposure time	0.5 ~ 25 ms
	Focal length	4.5 ~ 12 mm

The UAV wind field measurement system adopted a triple-direction wind field wireless sensor network measurement system [14], which consisted of a wind speed sensor module, a microprocessor and a wireless transmission module, a power module, and a host computer module. The wind speed sensor (Figure 1c) adopted the GM8904 digital interface impeller anemometer. After power-on, it connected with the microprocessor through the serial port to send wind speed data, wind temperature, and other data. The anemometer protocol stipulated the communication protocol for command control and data exchange between the lower computer and the upper computer (computer or smart device), and adopted the UART specification. The wind speed sensor collected and measured the triple-direction wind speed data of each wind field sampling node. The wind speed measurement range was 0~45 m/s, and the measurement accuracy was $\pm 3\%$. The CC2530F256 combined with the ZigBee protocol stack was selected as the microprocessor and wireless transmission module.

The UAV remote sensing simulation platform (Figure 2) consisted of horizontal and vertical guide rails, which could control the horizontal displacement speed and vertical height. Two servo motors were used to achieve precise control of horizontal and vertical movement speed. The platform had a

maximum load of 50 kg, which could counter the lift generated by the rotor rotation of the drone and meet the load-bearing requirements of the drone equipment.

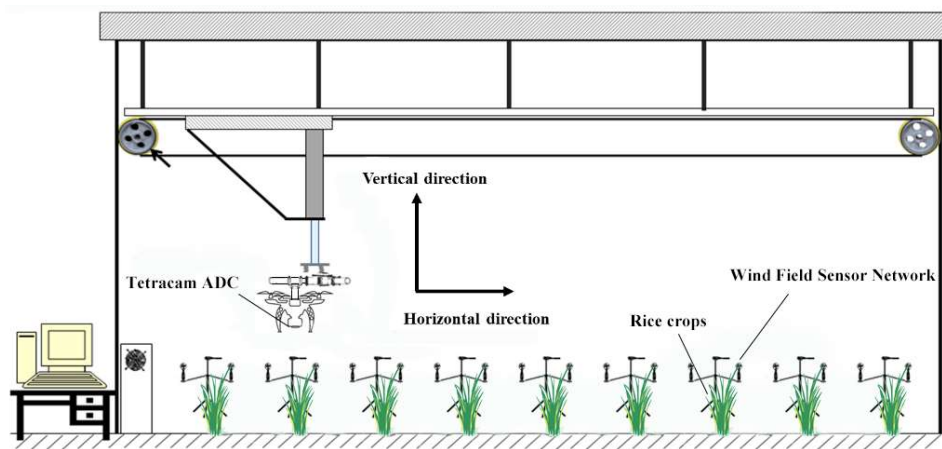


Figure 2. UAV remote sensing simulation platform system.

2.3. Data Acquisition

The horizontal line array was placed with nine groups of wind field wireless sensor network measurement nodes (Figure 3a), and each node was 30 cm apart. The height of the measurement node was set to 50 cm above the ground, and each node was equipped with three wind speed sensors. The mounting direction of the sensor axis is shown in Figure 3b, where the X direction was perpendicular to the row direction of the rice, the Y direction was parallel to the row direction of the rice, and the Z direction was perpendicular to the ground direction.

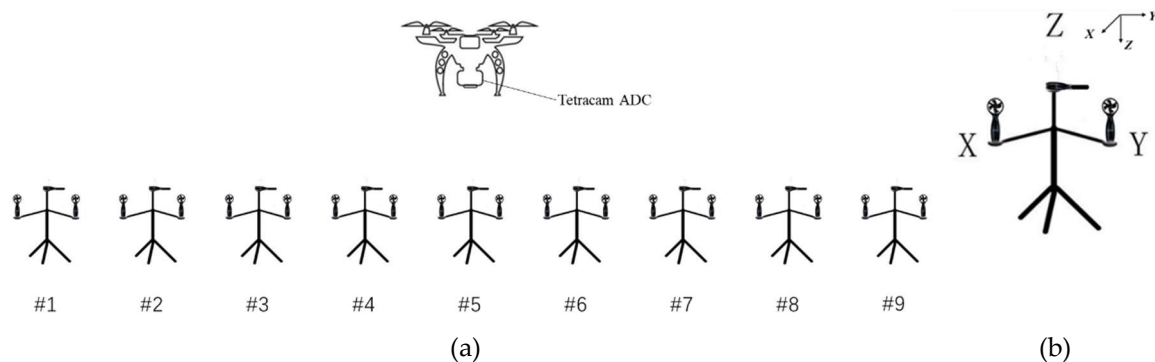


Figure 3. Schematic diagram of the device and distribution of the UAV wind field measurement node: (a) Distribution of line array wind field; (b) schematic diagram of the measurement nodes.

The Tetracam ADC multispectral camera was used as the image acquisition sensor, and the camera was mounted directly under the UAV to take an ortho-image of the crop canopy, at which time the rotor height was 145 cm above the ground.

Wind field data was measured at 6 height levels (145 cm, 155 cm, 165 cm, 175 cm, 185 cm, and 195 cm above ground) separately, while the UAV kept hovering above the rice crops. The throttle channel was always at the maximum value of 1860 μ s (rotor reached the maximum speed). For each height level, when the rotor reached a stable speed, wind field data in different directions were collected for 90 seconds, which would be processed into the final wind field matrix. In the meantime, the Tetracam ADC started taking pictures. Considering the overlap and massive duplication of images, images were only taken at nodes #1, #3, #5, #7, and #9, respectively, and 6 to 10 pictures were acquired for each node under wind field. As a control group, images of rice canopies at each measurement point were taken at a height of 145 cm in the absence of wind.

The upper limit of the acquisition frequency of the triple-direction wind speed sensor was 2 Hz, and one coordinator could receive data from up to 14 terminals during the test. Under the external interference, the data may get lost during the process of sending and receiving. In addition, the experiment roughly defined the wind speed value measured by the three anemometers as the single-point triple-direction wind speed value. However, the size of the anemometer itself could not be neglected. Therefore, interference between the anemometer and the bracket would have some impact on measurement results.

2.4. Data Processing

2.4.1. Image Data Processing

Images in a 10-bit depth, three-channel DCM format were captured by a Tetracam ADC multispectral camera, and the images were processed using PixelWrench 2 (Tetracam Inc., Chatsworth, CA, USA), Envi 5.1 (Harris Geospatial Solutions, Inc., Herndon, VA, USA), and Matlab R2018a (The MathWorks, Inc., Natick, MA, USA).

Considering the difference in soil and crop spectral reflectance in the NIR band, the appropriate threshold could be used to segment the crop canopy and soil background [20–24].

To perform image binarization, the segmentation threshold T between the background and the crop was selected according to the NIR band image. The portion with the DN value smaller than T was set as 0, and the portion with the T value larger than T was set as 255 according to the following equation:

$$g(x,y) = \begin{cases} 0, & f(x,y) < T \\ 255, & f(x,y) \geq T \end{cases} \quad (1)$$

where T was the threshold value of binarization, $f(x,y)$ was the original image, and $g(x,y)$ was the image after binarization.

After obtaining the binary image, masking process and region of interest (ROI) selection were carried out to obtain the three-channel (NIR, Red, and Green) images of the crop canopy area. The specific operation process is given in Figure 4.

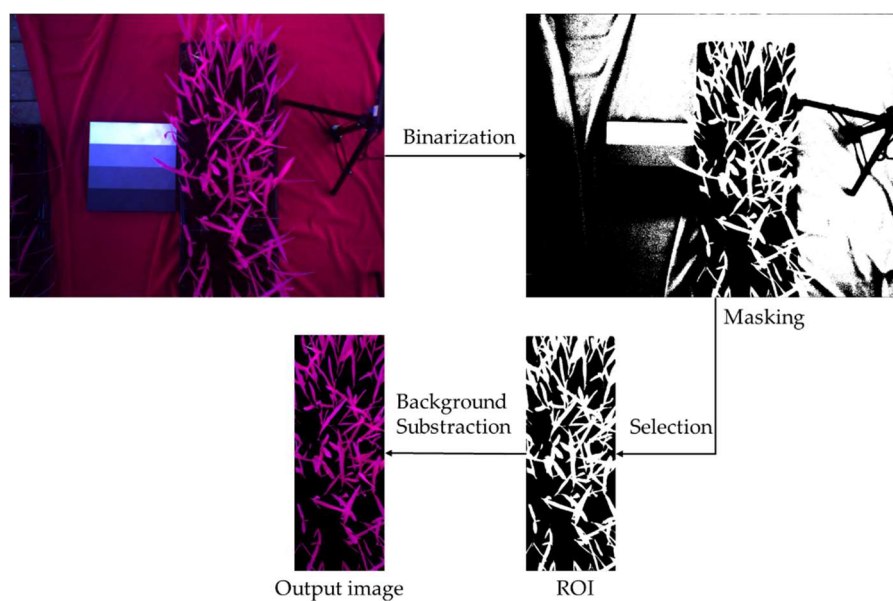


Figure 4. Image binarization, ROI (Region of Interest) extraction, and masking.

For the extraction and analysis of the image information, the gray density of the image and vegetation indices of rice crops was calculated. In this study, NDVI (Normalized Difference Vegetation

Index), RVI (Ratio Vegetation Index), and CCR (Canopy Coverage Rate) were chosen as the indices to tell the difference of spectral and posture information of rice crop canopy under different wind fields.

NDVI is linearly related to vegetation distribution density, which is the most widely used indicator of plant growth status and spatial distribution density of vegetation. As for RVI [25–28], the RVI value of the green healthy vegetation coverage area is much larger than 1, while the RVI value of the ground without vegetation cover is about 1, so RVI is a sensitive indicator parameter of green plants, which has a high correlation with LAI (leaf Area index), leaf dry biomass, and chlorophyll content, so we can estimate the biomass of rice crops by calculating RVI. The NDVI and RVI could be obtained according to the following equations:

$$NDVI = \frac{R_{NIR} - R_{RED}}{R_{NIR} + R_{RED}} \quad (2)$$

$$RVI = \frac{R_{NIR}}{R_{RED}} \quad (3)$$

where R_{NIR} and R_{RED} were reflectance values in NIR and RED bands, respectively.

CCR of rice crop refers to the ratio of rice canopy to the entire picture in remote sensing images, which could be calculated through the following equation:

$$CCR = \frac{\sum \text{Canopy pixel}}{\text{No. of pixels}} \quad (4)$$

where $\sum \text{Canopy pixel}$ was the sum of canopy pixels, and No. of pixels is the number of pixels of the entire image.

Studying the relationship between CCR and Z-direction wind speed could more directly explain the influence of UAV wind field on the acquisition of spectral information.

2.4.2. Radiometric Calibration

In order to obtain the reflectance of the rice canopy, it is necessary to perform radiometric calibration on the image [29–32]. Radiometric calibration is a process of converting the dimensionless Digital Number (DN) value recorded by the sensor into an atmospheric top radiance or reflectance that has an actual physical meaning. The principle of radiation correction is to establish a quantitative relationship between the digital quantized value and the radiance value in the corresponding field of view to eliminate the error generated by the sensor itself.

The gray level of the image obtained by remote sensing is proportional to the energy radiated by the object. The gray value of the object in an image is determined by the incident light intensity and reflectivity, which can be presented as the following equation:

$$f(x, y) = I(x, y) \cdot R(x, y) \quad (5)$$

where $f(x, y)$ is the acquired image, $I(x, y)$ is the ambient light, $R(x, y)$ is the object reflectance.

The gray value density of the reference panel area in the image is calculated by the following equation:

$$\text{Density of gray value} = \frac{\sum \text{gray value}}{\text{No. of pixels}} \quad (6)$$

To obtain the reflectance of the rice canopy, the regression model as follows needs to be established. In this study, the linear regression model can be obtained by least squares fitting.

$$Ref_a = \alpha_i \times DN_a + \beta_i \quad (7)$$

where Ref_a is the reflectance of the a -th gradient panel on the reference panel, DN_a is the DN of the a -th gradient panel on reference panel, α_i is the gain of the i -th band, and β_i is the offset value of the i -th band representing the response introduced by ambient radiation.

The spectral reflectance of the reference panel at different bands is presented in Figure 5. Combined with the DN data calculated from the spectral pictures, the correction models of image DN value and reference panel reflectance were built to obtain the reflectance of plant canopy. The model calculation results under NIR band are presented in Table 2. Determination of coefficient of all these models ranges from 0.9545 to 0.9998, which implied that these models had good performances on fitting the correlation between DN values and reflectance.

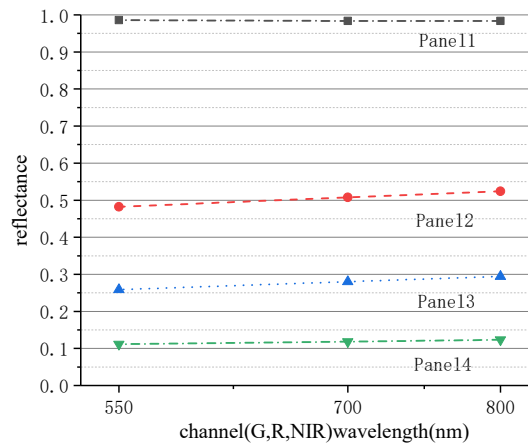


Figure 5. Reflection of the radiometric calibration panel at different wavelengths.

Table 2. Image DN value and reference panel reflectance correction model under NIR band.

Serial Number	Condition	Model	R ²
1	uw ¹	$y = 158.67x + 23.578$	0.9915
	w ²	$y = 84.473x + 1.2496$	0.9995
3	uw	$y = 170.69x + 20.618$	0.9977
	w	$y = 96.419x - 3.1504$	0.9951
5	uw	$y = 163.91x + 14.375$	0.9988
	w	$y = 44.744x + 1.5204$	0.9998
7	uw	$y = 121.78x + 21.037$	0.9973
	w	$y = 215.87x - 26.388$	0.9545
9	uw	$y = 160.09x + 30.238$	0.996
	w	$y = 227.7x - 19.085$	0.9783

Note: ¹ uw represents static measurement (UAV rotors keep static); ² w represents dynamic measurement (UAV kept hovering under the altitude of 145 cm).

2.4.3. Wind Field Data Processing

The wind speed measurement was carried out by using the triple-direction line array arrangement scheme, and the wind speed values of the same point on the ground (parallel flight direction X, vertical flight direction Y, and vertical direction Z) were measured when the UAV was hovering at different altitudes.

The wind speed data was transformed into a 60×27 wind field matrix. There were 60 rows of data in wind field matrix, where a single-row data recorded the wind speed values collected by 9 different sampling nodes. The row data described the data distribution of 27 impellers at the same time in a two-dimensional plane along the wind speed value axis and the sampling node number axis. There were a total of 27 columns of data in the wind field matrix, corresponding to the data changes of the 27 impellers in the experiment. The column data described the data variations of the same impeller in a two-dimensional plane along the numerical and time axis of the wind speed.

3. Results

3.1. Qualitative Comparison

After binarization and masking of the experimental images in different areas of the wind field, the image processing results were shown in Figure 6. The image darkened obviously in the windy condition due to ambient light changes during the experiment, which had a slight impact on the reflectance results. In addition, the exposed part of the soil in the image increased significantly, the coverage of the canopy of the rice decreased, and the canopy of the rice showed an obvious lodging posture in the case of wind.

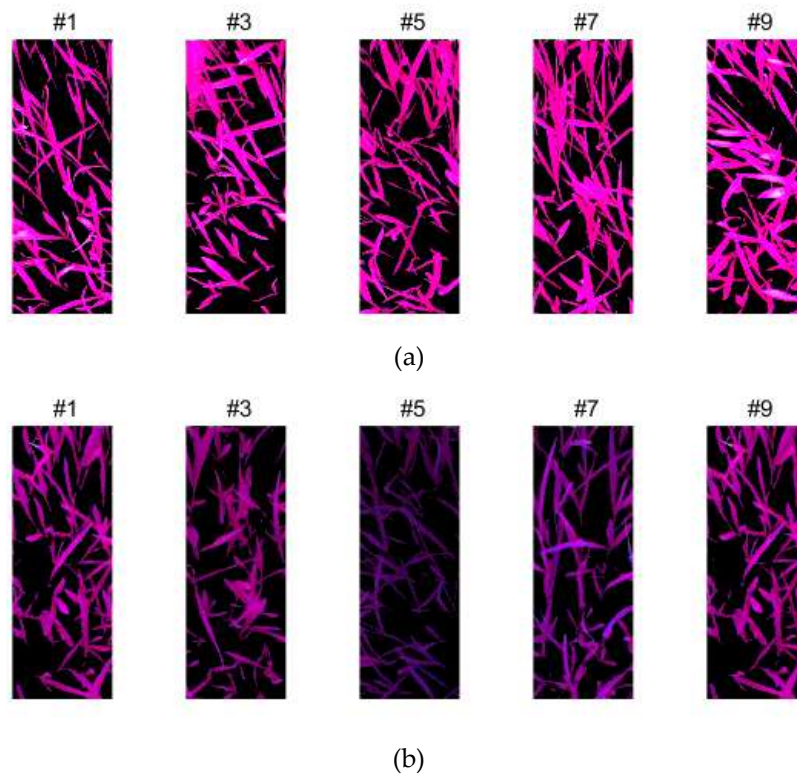


Figure 6. Comparison of windy and windless images at each measuring node: (a) static shooting while rotors keep still; (b) dynamic shooting under wind field at the altitude of 1.45 m.

The gray value densities of the rice canopy under each channel are recorded in Figure 7. It could be seen from the figure that rice canopy had the largest gray density value in the NIR band among the three bands, the GREEN band was the second largest, while the RED band was the smallest. This was because the spectral reflectance of the rice canopy in the NIR and GREEN bands was higher, while in the RED band, most of the light was absorbed by the rice canopy. Under the three bands, the gray density value in the absence of wind at the same sampling node was greater than the gray density value in the windy situation. Thus, the wind field had an obvious influence on the collection of spectral information.

3.2. Wind Field Description

3.2.1. Row Data of Wind Field Matrix

Figure 8 presented the maximum and average distribution of the triple-direction wind speed at the UAV hovering height of 145 cm. As seen from the graph, the average and maximum wind speed in the Z direction were the largest among three directions; the wind speed values in the X and Y directions were relatively small, mostly below 1 m/s. In addition, among all the wind speed sampling

nodes, the wind speed value of the No. 5 sampling node was the largest, and gradually decreased at both sides, but the wind speed values on both sides were not completely symmetrically distributed. The rate of wind speed drop on the side of the No. 9 sampling node was significantly faster than the other side, which might be the result of the interference with air flow at different locations in the confined space.

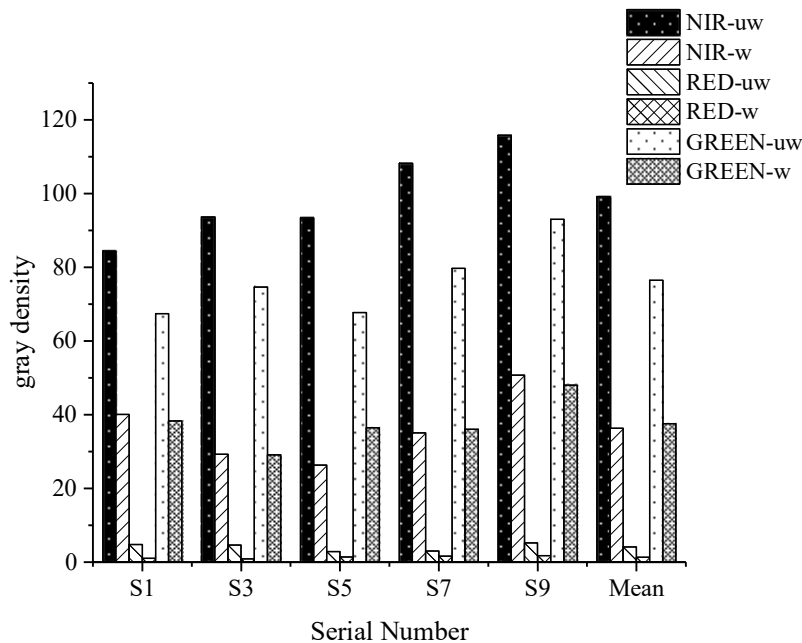


Figure 7. Gray value density of three-channel (NIR, R, and G) image. Note: uw-static measurement (UAV rotors keep static); w-dynamic measurement (UAV kept running under the altitude of 145 cm).

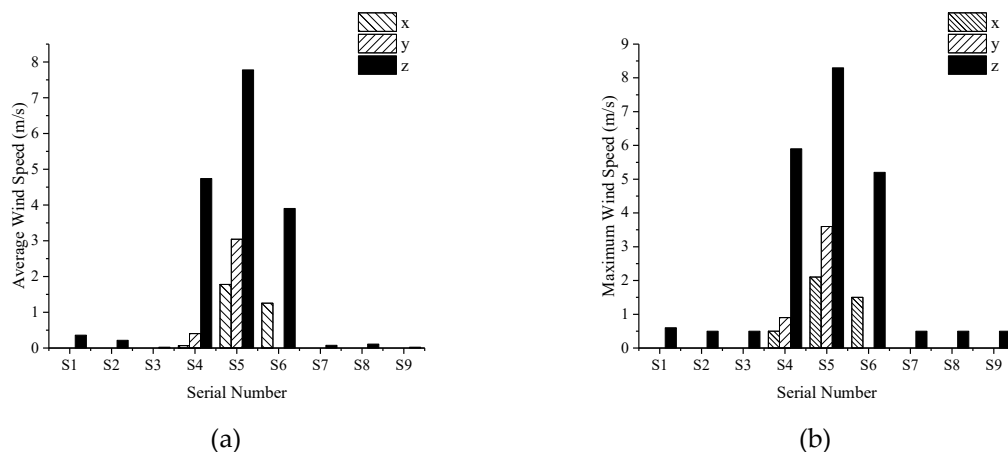


Figure 8. (a) The distribution of triple-direction average wind speed. (b) The distribution of triple-direction maximum wind speed.

3.2.2. Column Data of Wind Field Matrix

The wind field matrix had a total of 27 columns of data, which corresponded to the data changes of the 27 impellers in the experiment. The column data described the data variation of the same impeller in a two-dimensional plane along the numerical and time axes of the wind speed. Figure 9 is a triple-direction wind speed-time chart, where (a) ~ (f) corresponded to the triple-direction wind speed timing chart of sampling node No. 5 at the hovering height of 145 ~ 195 cm above ground (every 10 cm for one level). It could be inferred from the following pictures that the wind speeds in the Z direction and the Y direction were consistent with the time series, while the X direction wind speed

was almost close to 0 with only slight fluctuations and the Z-direction wind speed was much larger than the wind speed in the X and Y directions.

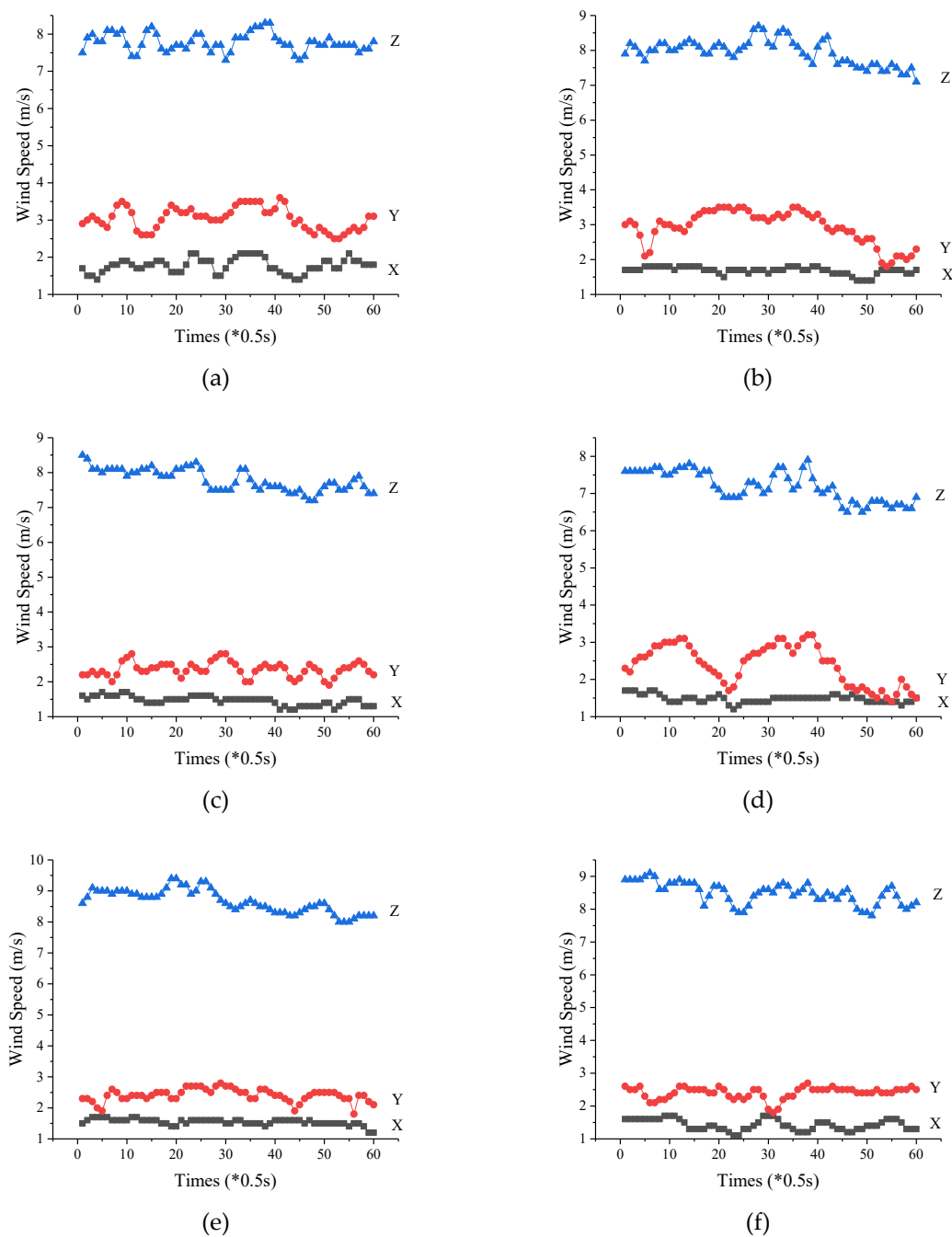


Figure 9. Triple-direction wind speed-time chart at different hovering heights: (a) 145 cm; (b) 155 cm; (c) 165 cm; (d) 175 cm; (e) 185 cm; (f) 195 cm.

3.2.3. Wind Field Contour Map

The distribution and width range of triple-direction wind field is shown in Figure 10. The hovering height of the UAV is 145 cm. The wind speed of X and Y direction at the height of 50 cm above the ground were close to zero on a large scale, and only partial wind field distribution of less than 2 m/s had a width of about 1 m. The Z-direction wind field presented a situation of decreasing diffusion from the center sampling node to both sides, and the wind speed value was higher near the center, but the wind field width range was smaller. The wind field had an approximate periodic variation

on the time axis. Therefore, the triple-direction wind field distribution contour map not only had the meaning of presenting the wind speed value in the row data and the column data, but also visually showed the distribution range and law of the wind field.

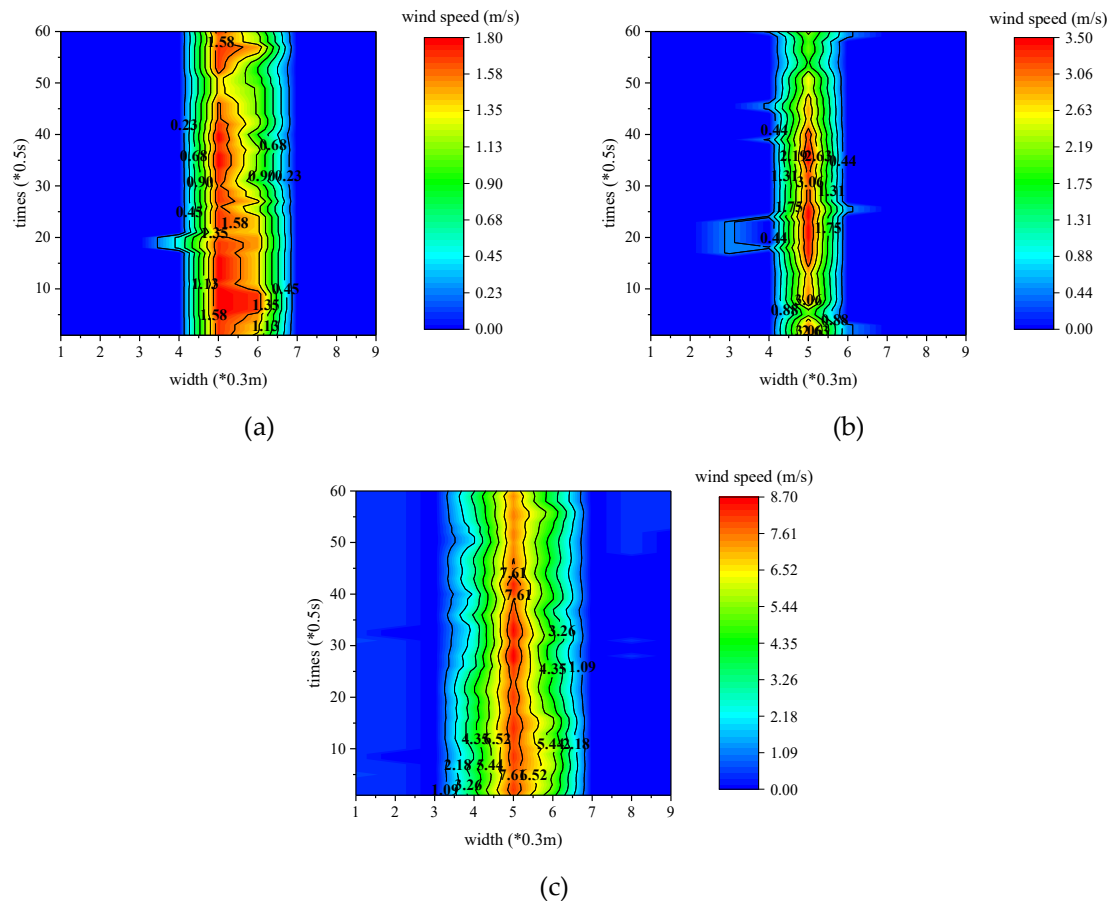


Figure 10. Contour map of triple-direction wind field: (a–c) represents the X, Y, Z wind field width contour map, respectively.

Based on the above finding, the study focused much more on the distribution of wind fields perpendicular to the ground direction (Z direction).

3.3. The Impact of Wind Field on NDVI

Crop information, such as vegetation indices and CCR, were calculated from images taken at different shooting points (corresponding to the serial number of wind speed measurement nodes). Figure 11 presented the scatter plot of NDVI-Wind Speed drawn from the data, and the data of node 5 was found to be abnormal value. This was because the wind speed of the UAV rotor wind field reached the maximum at the position of node 5. It dropped to both sides rapidly showing a steep wall effect [15]. Due to the scale of the wind speed sensing network device, this experiment could not capture the wind speed value data in the mid-range, thus most of the data were gathered in the area where the wind speed was small. Therefore, aside from the data of the central node, we focused on the law of the wind field on the NDVI in the low-speed wind field area.

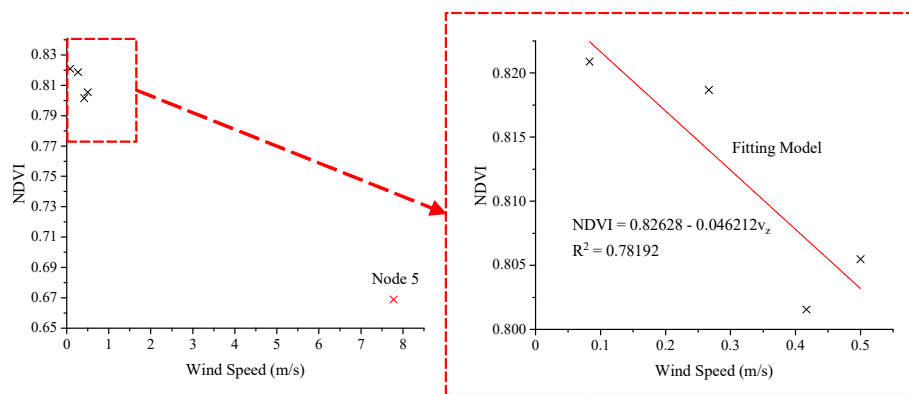


Figure 11. Scatter plot and linear regression model of NDVI (Normalized Difference Vegetation Index)-Wind Speed (Z direction).

The linear regression analysis result based on the low-speed wind field area data was also presented in Figure 11, and the regression model between the vegetation index NDVI and the wind speed v_z was as follows:

$$NDVI = 0.826 - 0.0462v_z \left(R^2 = 0.782 \right) \tag{8}$$

In this model, the value of the canopy vegetation index NDVI was negatively correlated with the Z-direction wind speed. This model indicates that the larger the Z-direction wind speed was, the smaller the NDVI coefficient was. NDVI is a kind of vegetation index that characterizes the growth of plants. The bigger the NDVI value was, the larger the coverage area of green plants was. When the Z-direction wind speed increased, the canopy surface of the rice would have a different degree of lodging and deformation, and the large area of the soil would be exposed. The NDVI index decreased along with the decrease of the coverage of the rice canopy. This experimental result was consistent with the actual observation.

The difference in NDVI values for different measurement nodes in the presence of wind and windless fields is showed in Figure 12. It can be clearly observed that the NDVI value of the No. 9 node in the windy case was slightly larger than that in the case of no wind. The NDVI values of the other nodes were smaller than those in the case of no wind. The wind speed of the wind field reached the maximum value at the No. 5 sampling node, and gradually decreased toward both sides, and the speed of the wind speed decreased from fast to gentle. Therefore, we could conclude that the larger the wind speed was, the smaller the corresponding NDVI value was, and where the wind speed changed rapidly, the NDVI value change was much larger.

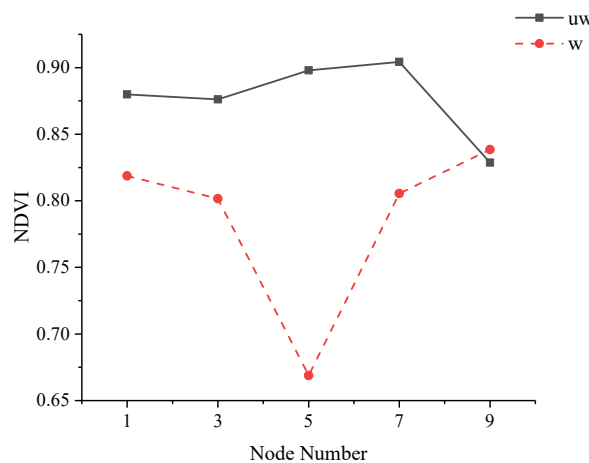


Figure 12. Comparison of NDVI value under windy and windless condition (uw-windless, w-windy).

3.4. The Impact of Wind Field on RVI

Figure 13 presents the scatter plot of RVI-Wind Speed drawn from the data, the same as NDVI, and the data of node 5 was found to be of an abnormal value. The Linear regression fitting model based on the low-speed wind field area data is also given by Figure 13.

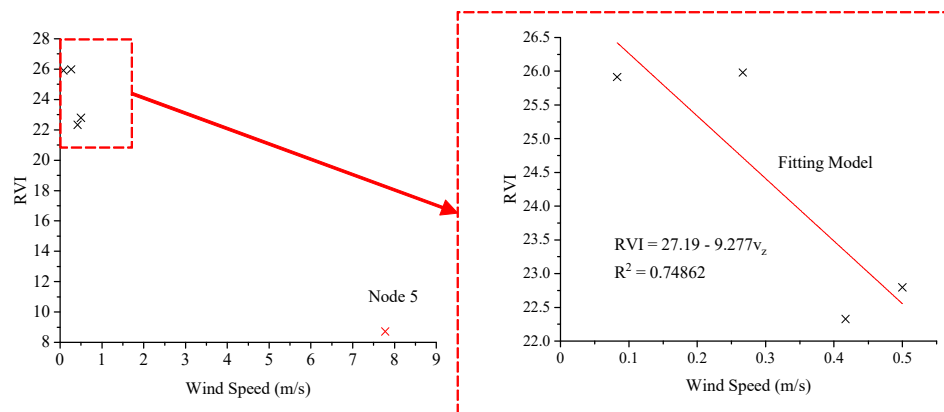


Figure 13. Scatter plot and linear regression model of RVI (Ratio Vegetation Index)-Wind Speed (Z direction).

For RVI, the regression model of the index RVI and the factor Z wind speed was presented as follows:

$$RVI = 27.19 - 9.277v_z \quad (R^2 = 0.74862) \quad (9)$$

The same as the NDVI model, the regression coefficient of the Z-direction wind speed was negative in this model, which indicated a negative correlation between RVI and Z-direction wind speed in the low-speed wind field area. The gain of the RVI model was much larger than that of NDVI, indicating that RVI was a more sensitive indicator parameter of green plants.

The difference between the RVI values under different measurement nodes in the presence of wind and windless fields is presented in Figure 14.

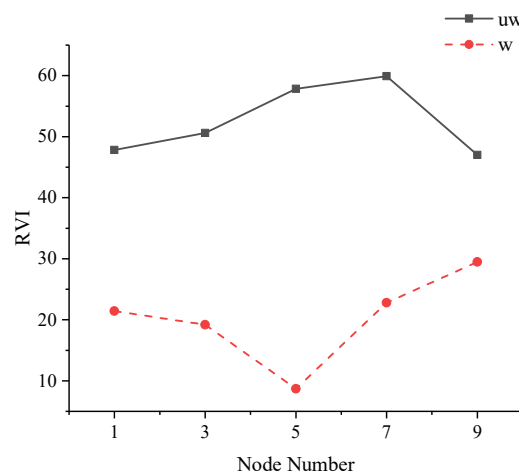


Figure 14. Comparison of RVI value under windy and windless condition (uw-windless, w-windy).

It can be found that the RVI values of the measured points were less than those in the absence of wind. Similar to NDVI, the larger the wind speed was, the smaller the corresponding RVI value was. Apparently, wind field had an effect on the RVI of rice canopy under the condition of this study.

3.5. The Impact of Wind Field on Rice Canopy Coverage Rate

The UAV rotor wind field would inevitably cause the lodging of rice crops, so CCR was chosen to describe the degree of the crop posture changes. The CCR of rice canopy under different shooting points was different, the difference between wind and windless CCR under each shooting point was selected to perform the regression analysis with Z-direction wind speed. The larger the $difference_{CCR}$ (CCR difference between windy and windless situation) was, the greater the impact of wind field on the CCR was. The dynamic CCR values (CCR_W) were subtracted from the static CCR values (CCR_{UW}) to obtain $difference_{CCR}$ and the equation to calculate $difference_{CCR}$ is as follows:

$$difference_{CCR} = CCR_{UW} - CCR_W \quad (10)$$

where CCR_{UW} represented the canopy coverage rate under windless condition, while CCR_W represented the canopy coverage rate under windy conditions.

Figure 15 presented the scatter plot of $difference_{CCR}$ - Wind Speed drawn from the data, the same as NDVI, the data of node 5 were found to be abnormal value. The linear regression fitting model based on the low-speed wind field area data is also presented in Figure 15.

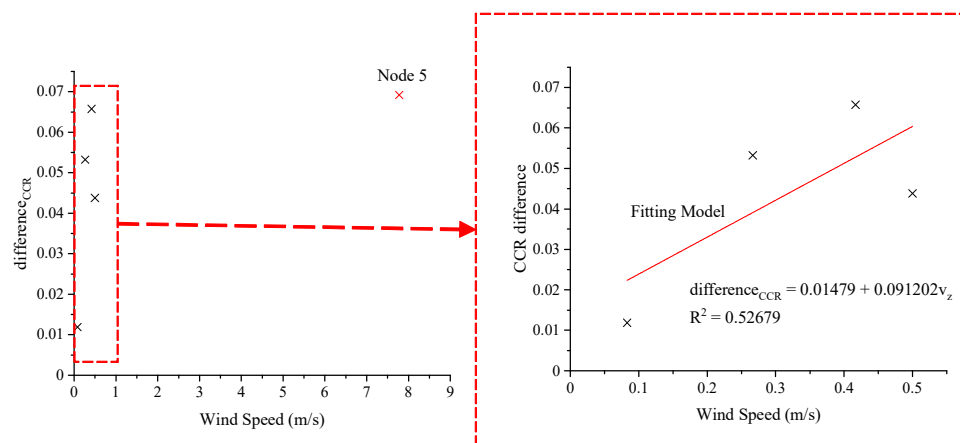


Figure 15. Scatter plot and linear regression model of $difference_{CCR}$ - Wind Speed (Z direction).

For $difference_{CCR}$, the relationship between the index RVI and the Z-direction wind speed could be described as follows:

$$difference_{CCR} = 0.01479 + 0.091202v_Z \quad (R^2 = 0.52679) \quad (11)$$

In this model, the regression coefficient of the Z-direction wind speed was positive, which indicated a positive correlation between $difference_{CCR}$ and Z-direction wind speed in the low-speed wind field area. This was because with the increase of Z-direction wind speed, the rice crop's canopy would have a different degree of lodging and deformation, and much more soil would be exposed, so that the value of CCR would go down, and the value of $difference_{CCR}$ would go up. However, when the wind speed kept growing larger, the limit of the rice canopy deformation would be reached, and the change of CCR gradually tended to be flat.

3.6. Variance Analysis

Variance analysis was conducted to explore the relationship between Z-direction wind speed and three indices (NDVI, RVI, and $difference_{CCR}$), and the results were presented in Table 3. From the results of variance analysis, it could be found that the significance level P of three linear regression models (NDVI, RVI, and $difference_{CCR}$) was 0.1154, 0.13477, and 0.2742, respectively. Therefore, the influence of Z-direction wind speed on NDVI, RVI, or $difference_{CCR}$ was not significant, though

the significance of level P was at least 0.05 in all cases. According to the above analysis, there is a correlation between Z-direction wind speed and the three indices, which is not just simple linear correlation, and this influence would eventually affect the real spectral image data acquisition and analysis in the practical operations. However, in the local wind field area, linear regression model can still be found as the general law of this correlation.

Table 3. Variance analysis of Z-direction wind speed and three indices.

Items	Sum of Squares	Mean Square	F	Sig.
NDVI	2.15×10^{-4}	2.15×10^{-4}	7.17108	0.11574
RVI	8.66829	8.66829	5.95609	0.13477
<i>difference_{CCR}</i>	8.38×10^{-4}	8.38×10^{-4}	2.22641	0.2742

4. Discussion

Multi-rotor UAVs are widely used in agriculture, making the UAV rotor wind field a significant factor affecting agricultural operations. The current research on the impact of wind field on agricultural operations was mostly limited to pesticides, fertilizer spraying, and pollination operations [15–18]. UAV low-altitude remote sensing could obtain much higher-resolution and clearer remote sensing images, from which more image details were obtained, so that we could control crop growth more accurately and explore its growth law [1–3]. The rotor wind field would inevitably cause the lodging, the posture, and even the spectral reflectance change of crops. Therefore, exploring the influence of the UAV wind field on the acquisition of low-altitude remote sensing information had practical significance for the research itself and the field operations.

This study aimed to explore the wind field distribution law of multi-rotor UAV and its influence on the collection of rice canopy spectral information (NDVI, RVI, etc.). In the triple-direction wind field of the line array, the trend of wind speed changing at each sampling node was basically the same under different heights, but the wind speed value in the Z direction was significantly larger than the X-direction and Y-direction wind speed values. Wang et al. [18] found that the wind speed values were ranked as V_X (X-direction wind speed) $> V_Y$ (Y-direction wind speed) $> V_Z$ (Z-direction wind speed) at different flight altitudes, and the wind speed continued to be stable. Chen et al. [17] found that the wind field in Z direction had a more significant impact on droplet deposition in aerial spraying than wind field in the X and Y directions. The different results were caused by the different flight parameters. In this study, a small F450 quadrotor was selected to keep hovering at a height under 2 m, while Wang et al. chose an unmanned single-rotor helicopter for research, and the flying height was 6, 7, 8, and 9 m. Chen et al. selected a M234-AT quadrotor flying at a height around 1.5 m. In general, the wind field had an approximate periodic variation on the time axis. The wind speed of X and Y direction at the height of 50 cm above the ground were close to zero at a large scale, and only partial wind field distribution of less than 2 m/s had a width of about 1 m. The wind speed below the rotor of the No. 5 sampling node was the largest among the nine sampling nodes, and the Z-direction wind field showed a decreasing trend from the No. 5 sampling node to both its sides. The closer the location to the center, the higher wind speed value was, while the smaller the wind field width was. Li et al. [33] found that the wind speed under the rotor of the UAV reached the maximum, and the rate of increase of the forward wind speed is significantly higher than that of the backward direction. The so-called “steep wall” of the entire wind field was symmetrical along the flight direction of the UAV, which was consistent with the wind distribution in this study. The variation of the width of the wind field at different heights was basically the same. The vicinity of the No. 5 sampling node was the area with the largest wind speed. The peak of the maximum wind field width at 185 cm reached 8.225 m/s, and the wind field width of the peak wind speed ranged from 0 to 0.3 m periodically. The wind speed in the region of 0.3 to 0.6 m away from the No. 5 sampling node was approaching zero, and the range of the global wind field width was in the range of 0.9 m to 1.2 m.

Variance and regression analysis of Z-direction wind speed and three indices (NDVI, RVI, and $difference_{CCR}$) were carried out to find the influence of wind field on spectral information of rice canopy. The data of node 5 was found to be an abnormal value, so we focused on the data at the low-speed wind field area, where linear regression models were built to describe the correlation. The R^2 of three linear regression models (NDVI, RVI, and $difference_{CCR}$) were 0.78192, 0.74862, and 0.52679, respectively. The significance level, p , of three linear regression models was 0.1154, 0.13477, and 0.2742, respectively. Therefore, the influence of Z-direction wind speed on the three indices of rice crop canopy was not significant, yet the multi-rotor UAV wind field does have an impact on the spectral information collection of rice canopy data. Although this effect is not significant, the trend of the effect was obvious. In this study condition, at the low-speed wind field area, the higher the Z-direction wind speed was, the smaller the value of NDVI and RVI were, and the larger the value of $difference_{CCR}$ was. Thus, when we use these indices to evaluate crop growth status and biomass, the Z-direction wind speed becomes a significant factor affecting the spectral index values, which may affect our assessment and decision-making on crop growth. Therefore, in the low-altitude remote sensing operation of UAVs, the influence of wind field on the acquisition of remote sensing information of rice crops needed to be considered. Li et al. [15] optimized the selection of UAV-assisted pollination parameters, including flight speed, mass of aircraft and load, and flight altitude. However, in this study, the multi-rotor UAV wind field data were collected when the rotors were perpendicular to the ground. However, in actual operations, the UAV will not always keep hovering all the time, so the parameters of the UAV, including the speed of flight, rotating speed of rotors, the rotor blade size, and flying attitude, will have an important impact on the wind field. The natural environmental factors such as natural wind, temperature, etc., can also become factors worth exploring, which needs further exploration in future research. Therefore, in order to obtain the real growth status of rice crops, it was necessary to further revise the various vegetation index indicators calculated through remote sensing images and taking more factors into consideration, and the models established in this study could help build the revised model and provide guidance for the actual operations.

5. Conclusions

In this study, the wind field of the F450 quadrotor UAV at different hovering heights was measured by a triple-direction wind field wireless sensor network system. Wind speed timing graph and the contour map of wind field width were drawn from the wind field matrix. In the meantime, the multi-spectral remote sensing images of the rice canopy were obtained at various sampling nodes, and indices for NDVI, RVI, and $difference_{CCR}$ were selected for the variance and regression analysis of the Z-direction wind speed in the wind field. Eventually, the satisfactory results of this study indicated that under the conditions of this experiment, the Z-direction and the Y-direction wind speed were consistent with the time series, and the Z-direction wind field of UAV rotors dominated along three directions. Under the influence of the environment, the wind field does not strictly obey the symmetric distribution, and the rate of wind speed drop on the side of the node 9 (in this study) was faster than the other side. The Z-direction wind field had an impact on rice canopy vegetation indices, such as NDVI and RVI, especially in the low-speed area. Although the effect is not significant, its influence could still eventually affect the assessment of rice growth status. In the future research, more factors (natural environmental factors and flight parameters) will be taken into consideration, and more samples and field experiments will be carried out to explore the specific rules of the influence on the rice canopy's spectral reflectance, which can be used to revise models built in this study and provide a theoretical basis for scientific detection and assessment of rice crop growth.

Author Contributions: L.F. and W.W. conceived and designed the experiment; W.W., J.W., and C.Z. performed the experiments; L.F., W.W., and C.Z. contributed to data analysis; L.F., W.W., C.Z., Y.Z., S.Z., and Y.H. analyzed the data and wrote the whole paper; all authors reviewed the manuscript.

Funding: This study was supported by National Key Research and Development Project (2016YFD0300606), Major science and technology projects in Zhejiang (2015C02007), and National Natural Science Foundation of China (61705195).

Conflicts of Interest: The authors declare no conflict of interest.

References

- Xiang, H.; Tian, L.J.B.E. Development of a low-cost agricultural remote sensing system based on an autonomous unmanned aerial vehicle (UAV). *Biosyst. Eng.* **2011**, *108*, 174–190. [[CrossRef](#)]
- Berni, J.A.; Zarco-Tejada, P.J.; Suárez Barranco, M.D.; Fereres Castiel, E. Thermal and narrow-band multispectral remote sensing for vegetation monitoring from an unmanned aerial vehicle. *IEEE Trans. Geosci. Remote Sens.* **2009**, *47*, 722–738. [[CrossRef](#)]
- Everaerts, J. The use of unmanned aerial vehicles (UAVs) for remote sensing and mapping. *Int. Arch. Photogramm. Remote Sens. Spat. Inf. Sci.* **2008**, *37*, 1187–1192.
- Zhang, X.L.; Liu, F.; He, Y.; Gong, X.Y. Detecting macronutrients content and distribution in oilseed rape leaves based on hyperspectral imaging. *Biosyst. Eng.* **2013**, *115*, 56–65. [[CrossRef](#)]
- Li, X.L.; He, Y. Discriminating varieties of tea plant based on Vis/NIR spectral characteristics and using artificial neural networks. *Biosyst. Eng.* **2008**, *99*, 313–321. [[CrossRef](#)]
- Dixon, D.; Boon, S.; Silins, U. Watershed-scale controls on snow accumulation in a small montane watershed, southwestern Alberta, Canada. *Hydrol. Process* **2014**, *28*, 1294–1306. [[CrossRef](#)]
- Kusnierek, K.; Korsaeath, A. Challenges in using an analog uncooled microbolometer thermal camera to measure crop temperature. *Int. J. Agric. Biol. Eng.* **2014**, *7*, 60.
- Langelaan, J.W.; Spletzer, J.; Montella, C.; Grenestedt, J. Wind field estimation for autonomous dynamic soaring. In Proceedings of the 2012 IEEE International Conference on Robotics and Automation, Saint Paul, MN, USA, 14–18 May 2012; pp. 16–22.
- Lee, K.; Han, Y.; Ha, J.-I. Dynamic model and control of wound-rotor machine in single-phase grid system. In Proceedings of the 2014 IEEE Applied Power Electronics Conference and Exposition—APEC 2014, Fort Worth, TX, USA, 16–20 March 2014; pp. 2719–2726.
- Ware, J.; Roy, N. An analysis of wind field estimation and exploitation for quadrotor flight in the urban canopy layer. In Proceedings of the 2016 IEEE International Conference on Robotics and Automation (ICRA), Stockholm, Sweden, 16–21 May 2016; pp. 1507–1514.
- Wang, L.; Zhou, Y.; Hua, D.X.; Wang, M. Theoretical Study and Simulation of Atmospheric Wind Field and Temperature Field Detection Based on Fabry-Perot Interferometer. *J. Opt. J.* **2011**, *31*, 9–14. (In Chinese)
- Li, H.; Zhang, Y. Research on Simulated Atmospheric Wind Field and Its Data Processing Technology. *J. Appl. Opt.* **2009**, *30*, 285–290. (In Chinese)
- Ren, J.B.; Shen, H.R. Analysis of Wind Measurement Error of UAV Pitot-Static Pressure Tube. *J. Equip. Command Technol. Coll.* **2004**, 45–48. (In Chinese)
- Hu, L.; Zhou, Z.Y.; Luo, X.W.; Wang, P.; Yan, Y.Z.; Li, J.Y. Design and Experiment of Wireless Sensor Network Measurement System for Unmanned Helicopter Wind Field. *J. Agric. Mach.* **2014**, *45*, 221–226. (In Chinese)
- Li, J.Y.; Zhou, Z.Y.; Hu, L.; Zang, Y.; Xu, S.; Liu, A.M.; Luo, X.W.; Zhang, T.M. Optimization of operation parameters for supplementary pollination in hybrid rice breeding using round multi-axis multi-rotor electric unmanned helicopter. *J. Agric. Eng.* **2014**, *30*, 1–9. (In Chinese)
- Li, J.Y.; Lan, Y.B.; Wang, J.W.; Chen, S.D.; Huang, C.; Liu, Q.; Liang, Q.P. Distribution law of rice pollen in the wind field of small UAV. *Int. J. Agric. Biol. Eng.* **2017**, *10*, 32–40.
- Chen, S.D.; Lan, Y.B.; Bradley, K.F.; Li, J.Y.; Liu, A.M.; Mao, Y.D. The influence of the wind field under the rotor of a multi-rotor UAV on the spray deposition of airborne droplets. *J. Agric. Mach.* **2017**, *48*, 105–113. (In Chinese)
- Wang, P.; Hu, L.; Zhou, Z.Y.; Yang, W.S.; Li, A.M.; Luo, X.W.; Xue, X.Y.; He, J.; Yan, Y.Z. Wind field measurement for supplementary pollination in hybrid rice breeding using unmanned gasoline engine single-rotor helicopter. *J. Agric. Eng.* **2013**, *29*, 54–61. (In Chinese)
- Zhang, Y.C.; Chen, Y.; Li, Y.J.; Liu, F.; He, Y. Rotor Simulation System for Rotorcraft Based on CAN Bus. *J. Agric. Mach.* **2018**, *49*, 108–115. (In Chinese)

20. Noh, H.K.; Zhang, Q.; Shin, B.-S.; Han, S. Multispectral image sensor for detection of nitrogen deficiency in corn by using an empirical line method. In Proceedings of the 2003 ASAE Annual Meeting, Las Vegas, NV, USA, 27–30 July 2003; American Society of Agricultural and Biological Engineers: St. Joseph, MI, USA, 2003; p. 1.
21. Noh, H.; Zhang, Q.; Shin, B.; Han, S.; Feng, L.J.B.E. A neural network model of maize crop nitrogen stress assessment for a multi-spectral imaging sensor. *Biosyst. Eng.* **2006**, *94*, 477–485. [[CrossRef](#)]
22. Pena-Barragan, J.M.; Ngugi, M.K.; Plant, R.E.; Six, J. Object-based crop identification using multiple vegetation indices, textural features and crop phenology. *Remote Sens. Environ.* **2011**, *115*, 1301–1316. [[CrossRef](#)]
23. Meyer, G.E.; Neto, J.C. Verification of color vegetation indices for automated crop imaging applications. *Comput. Electron. Agric.* **2008**, *63*, 282–293. [[CrossRef](#)]
24. Kastens, J.H.; Kastens, T.L.; Kastens, D.L.; Price, K.P.; Martinko, E.A.; Lee, R.-Y. Image masking for crop yield forecasting using AVHRR NDVI time series imagery. *Remote Sens. Environ.* **2005**, *99*, 341–356. [[CrossRef](#)]
25. Zhou, Z.; Plauborg, F.; Thomsen, A.G.; Andersen, M.N. A RVI/LAI-reference curve to detect N stress and guide N fertigation using combined information from spectral reflectance and leaf area measurements in potato. *Eur. J. Agron.* **2017**, *87*, 1–7. [[CrossRef](#)]
26. Jordan, C.F. Derivation of leaf-area index from quality of light on the forest floor. *Ecology* **1969**, *50*, 663–666. [[CrossRef](#)]
27. Dobrowski, S.Z.; Ustin, S.L.; Wolpert, J.A. Remote estimation of vine canopy density in vertically shoot-positioned vineyards: Determining optimal vegetation indices. *Aust. J. Grape Wine Res.* **2002**, *8*, 117–125. [[CrossRef](#)]
28. Colwell, J.E. Vegetation canopy reflectance. *Remote Sens. Environ.* **1974**, *3*, 175–183. [[CrossRef](#)]
29. Montanaro, M.; Lunsford, A.; Tesfaye, Z.; Wenny, B.; Reuter, D. Radiometric Calibration Methodology of the Landsat 8 Thermal Infrared Sensor. *Remote Sens.* **2014**, *6*, 8803–8821. [[CrossRef](#)]
30. Chen, Y.P.; Sun, K.M.; Li, D.R.; Bai, T.; Huang, C.Q. Radiometric Cross-Calibration of GF-4 PMS Sensor Based on Assimilation of Landsat-8 OLI Images. *Remote Sens.* **2017**, *9*, 811. [[CrossRef](#)]
31. Wang, C.Y.; Myint, S.W. A Simplified Empirical Line Method of Radiometric Calibration for Small Unmanned Aircraft Systems-Based Remote Sensing. *IEEE J. Sel. Top. Appl. Earth Obs. Remote Sens.* **2015**, *8*, 1876–1885. [[CrossRef](#)]
32. Liu, Y.K.; Ma, L.L.; Wang, N.; Qian, Y.G.; Qiu, S.; Li, C.R.; Tang, L.L. Vicarious radiometric calibration/validation of Landsat-8 operational land imager using a ground reflected radiance-based approach with Baotou site in China. *J. Appl. Remote Sens.* **2017**, *11*, 044004. [[CrossRef](#)]
33. Li, J.Y.; Zhou, Z.Y.; Lan, Y.B.; Hu, L.; Zang, Y.; Liu, A.M.; Luo, X.W.; Zhang, T.M. Distribution law of canopy wind field in rotary-wing UAV pollination operation. *J. Agric. Eng.* **2015**, *31*, 77–86. (In Chinese)



© 2019 by the authors. Licensee MDPI, Basel, Switzerland. This article is an open access article distributed under the terms and conditions of the Creative Commons Attribution (CC BY) license (<http://creativecommons.org/licenses/by/4.0/>).